Aspects of Three-Dimensional Imaging by Classical Tomography for Dual Detector Positron Emission Mammography (PEM)

Mark F. Smith[1], Stan Majewski[1], Andrew G. Weisenberger[1], Raymond R. Raylman[2],
Douglas A. Kieper[1], Joseph D. Kalen[3], Panos P. Fatouros[3]

[1]Thomas Jefferson National Accelerator Facility
Newport News, VA 23606, USA

[2]Center for Advanced Imaging, Department of Radiology, West Virginia University
Morgantown, WV 26506, USA

[3]Department of Radiology, Virginia Commonwealth University Health System
Richmond, VA 23298, USA

Submitted to *Physics in Medicine and Biology*
December 20, 2001

Corresponding Author:

Mark F. Smith, Ph.D.
Jefferson Lab
12000 Jefferson Avenue
Mail Stop 12H
Newport News, VA 23606
USA

Phone: (757) 269-5539
FAX: (757) 269-5235
E-mail: mfsmith@jlab.org

Short Title: Three-Dimensional Classical Tomography for PEM

Abstract

Images from dual detector positron emission mammography (PEM) systems are commonly reconstructed by backprojection methods of classical tomography. Characteristics of three-dimensional (3-D) PEM images were investigated using analytic models, computer simulations, and experimental acquisitions with compact pixellated detectors, in particular depth resolution normal to the detectors. An analytic formula was developed using circular image pixels that models blurring normal to the detectors. The amount of blurring is dependent on the acceptance angle for coincidence events and may vary across the field of view due to geometric limitations on the maximum angle of lines of response normal to the detectors. For experimental acquisitions with line sources and a pixellated lutetium gadolinium oxyorthosilicate (LGSO) detector, depth resolution is broader than predicted by numerical simulations, possibly due to uncorrected randoms or scatter within the scintillator arrays. Iterative image reconstruction with the maximum likelihood expectation maximization (MLEM) algorithm of a compressed breast phantom acquisition with a pixellated gadolinium oxyorthosilicate (GSO) detector shows improved contrast compared with backprojection reconstruction. Image reconstruction for dual detector PEM with static detectors represents a case of limited angle tomography with truncated projection data, and there is the opportunity to improve three-dimensional PEM imaging by the use of more sophisticated image reconstruction techniques.

1. Introduction

Positron emission mammography (PEM) with F-18 fluorodeoxyglucose (FDG) using conventional PET scanners has the capability to image regions of increased metabolic activity in the breast, which may prove useful in the detection, staging and treatment of breast cancer (Wahl *et al* 1991, Adler *et al* 1993, Avril *et al* 1999, Yutani *et al* 1999, Avril *et al* 2000, Yap *et al* 2001). Tomographic imaging of breast tumors with FDG and a gamma camera equipped with high energy collimators also has been investigated (Holle *et al* 1996). Histological and immunohistochemical analysis of breast carcinomas shows that there is no single explanation for the variation of FDG uptake in breast tumors (Avril *et al* 2001).

Several groups, including our own, have built or are developing dedicated PEM imaging systems in an effort to achieve better sensitivity and resolution than is attainable with general purpose PET systems. System designs include small parallel planar detectors (Thompson *et al* 1994, Weinberg *et al* 1996, Freifelder and Karp 1997, Doshi *et al* 2000, Raylman *et al* 2000), curved plate detectors (Hutchins and Simon 1995, Freifelder *et al* 1998), small ring configurations (Hutchins and Simon 1995, Freifelder and Karp 1997, Baghaei *et al* 2000) and rectangular box designs (Moses *et al* 1995, Huesman *et al* 2000). Initial clinical evaluations have been reported for two of the dual planar detector PEM systems (Murthy *et al* 2000, Adler *et al* 2001).

With dual detector PEM the breast is imaged between two static parallel planar detectors. The most commonly used image reconstruction method is the backprojection method of classical tomography, in which images are formed in planes parallel to the detectors (Anger and Rosenthal 1959, Barrett and Swindell 1981). Image reconstruction also has been implemented by 2-D iterative reconstruction in planes perpendicular to the detectors after single slice rebinning for a PEM simulation (Freifelder and Karp 1997). For both reconstruction methods there is blurring between the detectors due to incomplete angular sampling in planes perpendicular to the detectors. More general approaches to limited angle tomography (Rangayyan *et al* 1985, Barrett 1990) could potentially be applied to dual parallel detector PEM.

The goal of this work is to provide a better understanding of some aspects of classical tomography reconstruction for 3-D PEM image formation. In particular, depth resolution and the appearance of images normal to the detectors will be investigated. Analytic and computer modeling will be used and results from physical experiments will be presented. A comparison with iterative image reconstruction also will be presented.

2. Analytic model

In this section an analytic model of angle-dependent point source sensitivity will be used to estimate the intensity of a point source in different reconstructed image planes. These intensities will be used to estimate resolution normal to the detectors.

2.1. Point source sensitivity

Consider a simple PEM detector model where the two planar detector heads are parallel and separated by a distance D (figure 1). Assume that each detector has an efficiency s for detection of an annihilation photon and that photons are detected at the front surface of the detectors. Also suppose that a point source of activity A (positron emissions/sec) is located at position P that is a distance L from one of the detector heads. Then the photon flux density from annihilation photons (counts/sec/unit area) on the surface of that detector is

$$f(r) = (A/(2\pi d^2))\cos\theta = (A/2\pi)(L/(L^2 + r^2)^{3/2}) \qquad (1)$$

where r is the distance from the orthogonal projection of point P onto the detector surface and θ is the angle from normal incidence. Equation (1) can be integrated for the photon flux within an acceptance angle $\theta_{\max}$ from normal incidence,

$$F(\theta_{\max}) = A(1-\cos\theta_{\max}) \tag{2}$$

where the acceptance cone is within the field of view of the detector.

The geometric efficiency for detection of annihilation events is $1-\cos\theta_{\max}$ and the total sensitivity is $s^2(1-\cos\theta_{\max})$ if the acceptance cones for both annihilation photons are within the fields of view of the detectors. Use of a larger acceptance angle in image reconstruction will increase sensitivity, which should decrease statistical noise in the resulting images and enable better detection of smaller and lower contrast tumors. Increasing the acceptance angle will degrade image uniformity (Raylman *et al* 2000) unless compensated for analytically or with the use of a uniformity scan from a phantom.

The effect of acceptance angle on sensitivity has been previously investigated and sensitivity across the field of view can be made more uniform by restricting the angular acceptance angle of coincidence events (Muehllehner *et al* 1976). Formulae for the spatial-dependent sensitivity of circular detectors in coincidence have been developed (Weathersby *et al* 1984).

2.2. Depth resolution for an ideal detector and circular pixels

Reconstructed images are formed in planes parallel to the detectors by backprojecting counts along the lines of response connecting the detection locations of the annihilation photons. The resulting images are the sum of a focused image of activity in the desired plane and blurred images of activity in other planes. The point spread function (PSF) normal to the detectors can be derived for the case of an ideal detector with arbitrarily small pixels and backprojection into circular image pixels.

In the image plane containing the point source, all events within the axial acceptance angle will contribute to the pixel containing the source point P (figure 2). Now consider a circular pixel of radius R that is located a distance z from the point source along a line perpendicular to the detector face. The maximum angle from the normal of annihilation photons originating at point P that pass through this circle is $\theta_z = \arctan(R/z)$. If the maximum acceptance angle for image reconstruction is $\theta_{\max}$, then the photon flux from point P contributing to reconstructed counts in this pixel is

$$F(\theta_z) = A\,(1 - \cos(\min\{\theta_z, \theta_{\max}\})) \tag{3}$$

The PSF perpendicular to the detector and normalized to unity at z=0 follows from equations (2) and (3) as

$$\begin{aligned} PSF(z) &= (1 - \cos(\min\{\theta_z, \theta_{\max}\}))/(1 - \cos\theta_{\max}) \\ &= \min\{(1 - 1/[1 + (R/z)^2]^{1/2})/(1 - \cos\theta_{\max}), 1\} \end{aligned} \tag{4}$$

A measure of the imaging resolution perpendicular to the detector face is given by the full-width at half-maximum (FWHM) of the PSF. From equation (4) this is

$$FWHM(\theta_{\max}) = R(1 + \cos\theta_{\max})/[1 - (1/4)(1 + \cos\theta_{\max})^2]^{1/2} \tag{5}$$

When the detector is discretized and image reconstruction is onto a grid of square pixels, the image counts in the focal plane of a point source are usually spread among several pixels in a manner that is dependent on the implementation of backprojection algorithm. The maximum pixel value in the image is a factor $\beta < 1$ times the total image counts and is also dependent on the location of the point source with respect to the discretization grid. For this more general case an expression for the PSF normal to the detectors has not yet been found, however empirically the FWHM of small point sources often can be modeled by

$$FWHM(\theta_{\max}) = 2R[1-(\beta/2)(1-\cos\theta_{\max})]/\{1-[1-(\beta/2)(1-\cos\theta_{\max})]^2\}^{1/2} \tag{6}$$

which reduces to equation (5) when β=1.

As an example, consider the case of circular pixels 3.39 mm in diameter (area 9 mm^2). The dependence of the PSFs on the maximum acceptance angle is shown in figure 3. The resolution normal to the detectors improves when the acceptance angle increases because the point sources are increasingly blurred in non-focal planes (figure 4).

3. Numerical simulations and physical experiments

3.1. *Point source*

Point source acquisitions were simulated numerically for a PEM system with pixellated detectors using ray-tracing and numerical integration methods. Photons were assumed to be detected at the surface of the detectors. The detector heads were modeled as 29 x 29 arrays of 3.3 mm pixels, the same geometry as PEM detectors we have built (Raylman *et al* 2000). The detector separation was 18 cm.

Image reconstruction was by classical tomography with a pixel size of 3.3 mm and image plane spacing of 3.3 mm. Images were reconstructed with acceptance angles of 5, 10, 15 and 20 degrees. Depth resolution improves with increasing acceptance angle, though there is considerable blurring normal to the detector (figure 5). The FWHM of vertical profiles through the point sources (figure 6) are 10.6, 5.2, 3.6 and 2.7 cm for 5, 10, 15 and

20 degree acceptance angles, respectively. The widths predicted by equation (6) with β = 0.29 are 11.2, 5.6, 3.7 and 2.8 cm, respectively.

3.2. Line source

Coincidence data were acquired with a PEM system built with a pixellated array of lutetium gadolinium oxyorthosilicate (LGSO) crystals (Hitachi, Inc.). Each detector head was 10 cm x 10 cm with a 29 x 29 crystal array; the individual crystals were 3 mm x 3 mm x 10 mm and the crystal pitch was 3.3 mm. The crystals were coupled to an array of 4 x 4 Hamamatsu R7600-00-C8 position sensitive photomultiplier tubes. The rest of the detector design has been described elsewhere (Raylman *et al* 2000). The acquisition energy window was 420-650 keV.

Three line sources were filled with F-18 and placed midway between the detector heads, which were separated by 18 cm. Images were reconstructed in the central 21 slices with a spacing of 3.3 mm using 10 and 20 degree acceptance angles. Blurring normal to the detectors is more severe for the smaller acceptance angle (figure 7). Depth resolution varies spatially because of the more limited angular range of lines of response near the edge of the detector. Depth resolution is broader than predicted by the numerical simulations, possibly due to uncorrected randoms or scatter within the scintillator arrays.

3.3. Breast phantom with tumors

A 6 cm thick box phantom simulating a compressed breast was filled with 33 nCi/cc F-18 and imaged for 10 min with the previously described PEM system. The distance between the detector heads was 7.5 cm. Simulated tumors 12 mm, 10 mm, 8 mm and 4 mm diameter were filled with activity in a 10:1 tumor:background activity concentration ratio. Images were reconstructed for 21 slices with a 3.3 mm spacing using a coincidence acceptance angle of 20 degrees. The three larger tumors are visible in their focal plane, but there is appreciable blurring normal to the detectors (figure 8).

3.4. Comparison of backprojection and iterative image reconstruction

Image reconstruction for dual detector PEM can also be performed by iterative image reconstruction. The matrix equation

$$\boldsymbol{d} = \boldsymbol{G}\, \boldsymbol{s} \tag{7}$$

can be solved for an estimate of the 3-D source distribution, $\boldsymbol{s}$, where $\boldsymbol{d}$ is a data vector whose elements are the coincidences along the lines of response and $\boldsymbol{G}$ is the system matrix. In this formulation there is no rebinning of the coincidence data into projections. Coincidence data were acquired for a 4 cm thick compressed breast phantom with 5, 9, 12 and 16 mm diameter lesions with a pixellated gadolinium oxyorthosilicate (GSO; Hitachi, Inc.) detector built with a 29 x 29 array of 3 x 3 x 10 mm^3 crystal elements with a pitch of 3.3 mm (Raylman *et al* 2000). The phantom was placed midway between the detectors, which were separated by 20 cm, as might be the case for radiotracer guidance of core biopsy. A total of 115,000 coincidence events were acquired in a 400-700 keV energy window.

Iterative reconstruction by the maximum likelihood expectation maximization (MLEM) method (Lange and Carson 1984) was compared with image reconstruction by classical tomography (figure 9). Contrast is improved with iterative reconstruction because it is a three-dimensional image reconstruction method that attempts to correctly estimate activity in each plane, in contrast to backprojection reconstruction that forms images by focusing and defocusing activity in different planes. This example shows potential benefits of iterative image reconstruction for PEM with static detectors, though additional work is needed to evaluate iterative reconstruction with respect to backprojection reconstruction.

4. Discussion

The analyses and simulations of this paper were simple ones that represent an initial effort toward quantifying blurring normal to the detectors for PEM where image reconstruction is performed by the backprojection method of classical tomography. Analytic expressions, numerical simulations and experimental acquisitions show that this blurring is a function of the acceptance angle for coincidence events, as expected. Depth resolution is poorer near the edge of the field of view of the detectors due to geometric limitations on the maximum possible angle of lines of response to the detector normal. Depth-dependent blurring as well as sensitivity, image uniformity and image noise are affected by the maximum acceptance angle used for reconstruction.

The analytic expression for the PSF normal to the detector could be improved by generalizing it to model discretization of the detectors and of the backprojected images. The numerical simulations could be made more realistic by better modeling photon interactions in the source region and detector and by modeling random and scatter events. Improved simulations may better model the observed depth resolution for experimental acquisitions.

Image reconstruction by classical tomography has advantages and disadvantages for dual detector PEM. One advantage is high sensitivity since all of the coincidence data within a given acceptance angle can be used in image reconstruction, reducing statistical noise. It is also fast enough that image reconstruction can be implemented in real-time with data acquisition (Weinberg *et al* 1996). The major disadvantage is that activity from neighboring planes is blurred into the image plane, not removed as for computed tomography.

This leads to the broader question of whether there are better methods for extracting 3-D information from coincidence data acquired with dual detector PEM. It may be possible to obtain improved images by the use of analytic limited angle tomographic methods, though for the case of dual detector PEM the projections obtained by rebinning the line of response (LOR) data are truncated. In this case it may be possible to write integral expressions for the spatial-dependent 3-D PSF using Fourier methods that include the effect of missing and truncated projection data. Iterative image reconstruction methods also merit further study.

A general challenge for PEM is the optimization of detector design (e.g. planar detectors, curved detectors, ring detectors), detector motion (static, few or many detector positions), image reconstruction method (classical tomography, computed tomography, iterative reconstruction), breast positioning (uncompressed vs. compressed) and other factors for desired detection or quantitation tasks.

5. Conclusion

Three-dimensional imaging for a dual detector positron emission mammography system has been investigated for image reconstruction by classical tomography, which is widely used for dual detector PEM image reconstruction. Analytic models and computer simulations of a PEM system provide insight into the blurring normal to the detectors observed in reconstructed PEM images from experimental line source and breast phantom acquisitions. Improved methods of extracting 3-D information from PEM coincidence data, possibly including iterative image reconstruction, would be beneficial.

Acknowledgments

The Southeastern Universities Research Association operates Thomas Jefferson National Accelerator Facility for the United States Department of Energy under contract

DE-AC05-84ER40150. This work is supported by the Office of Biological and Environmental Research of the Office of Science of the U.S. Department of Energy and by grant 1 R21 CA82752-01 from the National Cancer Institute of the National Institutes of Health.

References

Adler L P, Crowe J P, Al-Kaisi N K and Sunshine J L 1993 *Radiology* **187** 743-50

Adler L P, Freimanis R I, Lesko N M, Bergman S, Geisinger K R, Levine E A, Perrier N, Newman D P, Sharpe C S, Williams R C, Zawarzin V and Weinberg I N 2001 *J. Nucl. Med.* **42** 81P

Anger H O and Rosenthal D J (1959) In *Medical Radioisotope Scanning* International Atomic Energy Agency, Vienna, pp 59-82

Avril N, Menzel M, Dose J, Schelling M, Weber W, Jänicke F, Nathrath W and Schwaiger M 2001 *J. Nucl. Med.* **42** 9-16

Avril N, Rosé C A, Schelling M, Dose J, Kuhn W, Bense S, Weber W, Ziegler S, Graeff H and Schwaiger M 2000 *J. Clin. Oncol.* **18** 3495-502

Avril N, Schelling M, Dose J, Weber W A and Schwaiger M 1999 *Clin. Pos. Imag.* **2** 261-71

Baghaei H, Wong W-H, Uribe J, Li H, Zhang N and Wang Y 2000 *IEEE Trans. Nucl. Sci.* **47** 1080-84

Barrett H H 1990 *J. Nucl. Med.* **31** 1688-92

Barrett H H and Swindell W (1981) *Radiological Imaging: The Theory of Image Formation, Detection and Processing,* Academic, New York

Doshi N K, Shao Y, Silverman R W and Cherry S R 2000 *Med. Phys.* **27** 1535-43

Freifelder R and Karp J S 1997 *Phys. Med. Biol.* **42** 2463-80

Freifelder R, Karp J S, Surti S and Wear J A 1998 *J. Nucl. Med.* **39** 171P

Holle L-H, Trampert L, Lung-Kurt S, Villena-Heinsen C E, Püschel W, Schmidt S and Oberhausen E 1996 *J. Nucl. Med.* **37** 615-22

Huesman R H, Klein G J, Moses W W, Qi J, Reutter B W and Virador P R G 2000 *IEEE Trans. Med. Imaging* **19** 532-37

Hutchins G D and Simon A J 1995 *J. Nucl. Med.* **36** 69P-70P

Lange K and Carson R 1984 *J. Assist. Comput. Tomogr.* **8** 306-16

Moses W W, Budinger T F, Huesman R H and Derenzo S E 1995 *J. Nucl. Med.* **36** 69P

Muehllehner G, Buchin M P and Dudek J H 1976 *IEEE Trans. Nucl. Sci.* **NS-23** 528-37

Murthy K, Aznar M, Thompson C J, Loutfi A, Lisbona R and Gagnon J H 2000 *J. Nucl. Med.* **41** 1851-58

Rangayyan R, Dhawan A P and Gordon R 1985 *Appl. Optics* **24** 4000-12

Raylman R R, Majewski S, Wojcik R, Weisenberger A G, Kross B, Popov V and Bishop H A 2000 *Med. Phys.* **27** 1943-54

Thompson C J, Murthy K, Weinberg I N and Mako F 1994 *Med. Phys.* **21** 529-38

Wahl R L, Cody R L, Hutchins G D and Mudgett E E 1991 *Radiology* **179** 765-70

Weathersby P K, Survanshi S S and Meyer P 1984 *Nucl. Instrum. Meth. Phys. Res.* **220** 571-74

Weinberg I, Majewski S, Weisenberger A, Markowitz A, Aloj L, Majewski L, Danforth D, Mulshine J, Cowan K, Zujewski J, Chow C, Jones E, Chang V, Berg W and Frank J 1996 *Eur. J. Nucl. Med.* **23** 804-06

Yap C S, Seltzer M A, Schiepers C, Gambhir S S, Rao J, Phelps M E, Valk P E and Czernin J 2001 *J. Nucl. Med.* **42** 1334-37

Yutani K, Tatsumi M, Shiba E, Kusuoka H and Nishimura T 1999 *J. Nucl. Med.* **40** 1003-08

Figure Captions

Figure 1. Diagram of the geometry of a point source P between two PEM detectors.

Figure 2. Diagram of circular pixels of radius R in different image planes.

Figure 3. Point spread functions normal to the detector for different maximum acceptance angles (θ_{max}) of coincidence events (equation (4)). An ideal detector is modeled and the circular image pixels are 3.4 mm in diameter.

Figure 4. Full-width at half-maximum of the PSFs normal to the detector as a function of the maximum acceptance angle of coincidence events contributing to the backprojection images (equation (5)). An ideal detector is modeled and the circular image pixels are 3.4 mm in diameter.

Figure 5. Images normal to the detector face for reconstructions of a point source with various acceptance angles. The detectors would be positioned at the top and bottom of each image.

Figure 6. Profiles normal to the detectors for a point source simulation and image reconstruction with different acceptance angles. The images corresponding to these curves are shown in Figure 5.

Figure 7. Images of line sources from an experimental acquisition for (a) 10 degree and (b) 20 degree acceptance angles. (left) Focal plane image parallel to the detectors, (center) image normal to the detectors and (right) vertical profile through the center line source of the image normal to the detectors. Only the center 21 slices spaced at 3.3 mm were reconstructed.

Figure 8. Images of a compressed breast phantom with simulated tumors from an experimental acquisition. Image reconstruction was with a 20 degree acceptance angle. (a) Focal plane image parallel to the detectors, (b) image normal to the detectors through the upper two tumors of (a), (c) image normal to the detectors through the tumors on the right side of (a), (d) vertical profile through the left tumor of (b), (e) vertical profile through the right tumor of (b).

Figure 9. Images of a compressed breast phantom reconstructed with (a) classical tomography (backprojection) and (b) iterative MLEM (5 iterations) methods. From left to right: image through the simulated lesions parallel to the detectors, horizontal profile through the upper 12 and 9 mm diameter lesions, image normal to the detectors through the 12 and 9 mm lesions and a vertical profile through the 12 mm lesion.

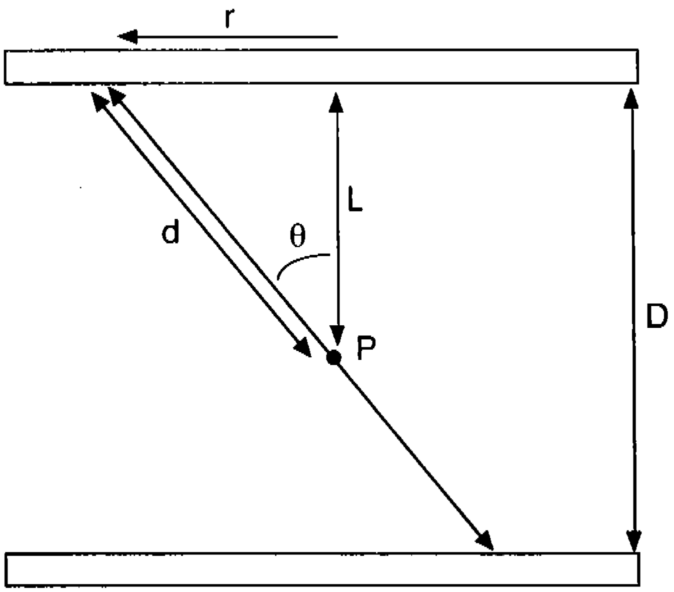

Figure 1. Diagram of the geometry of a point source *P* between two PEM detectors.

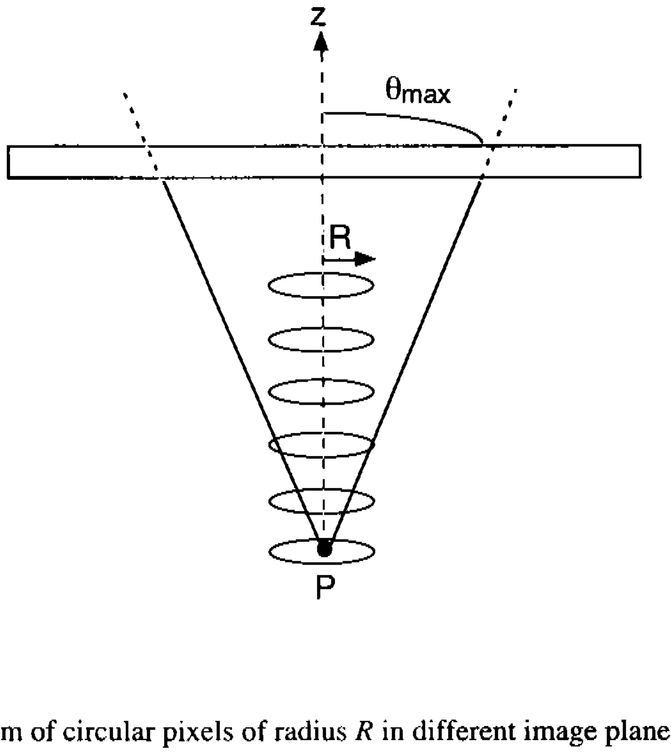

Figure 2. Diagram of circular pixels of radius *R* in different image planes.

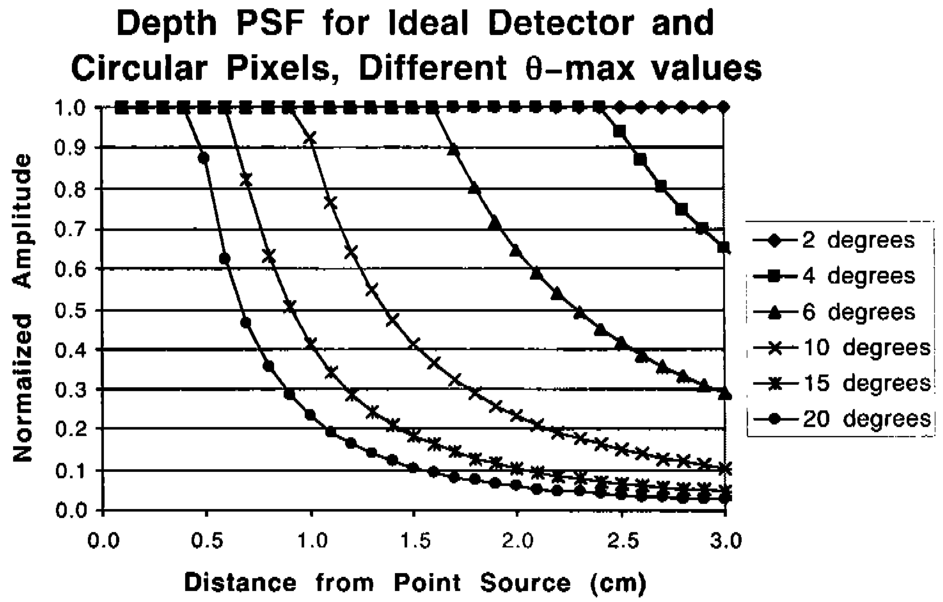

Figure 3. Point spread functions normal to the detector for different maximum acceptance angles ($\theta_{\max}$) of coincidence events (equation (4)). An ideal detector is modeled and the circular image pixels are 3.4 mm in diameter.

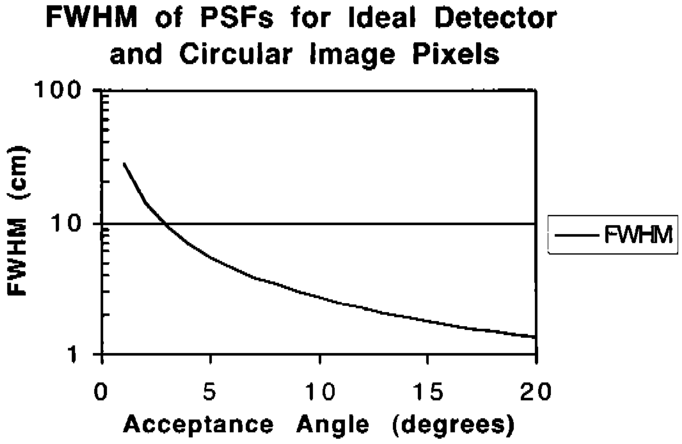

Figure 4. Full-width at half-maximum of the PSFs normal to the detector as a function of the maximum acceptance angle of coincidence events contributing to the backprojection images (equation (5)). An ideal detector is modeled and the circular image pixels are 3.4 mm in diameter.

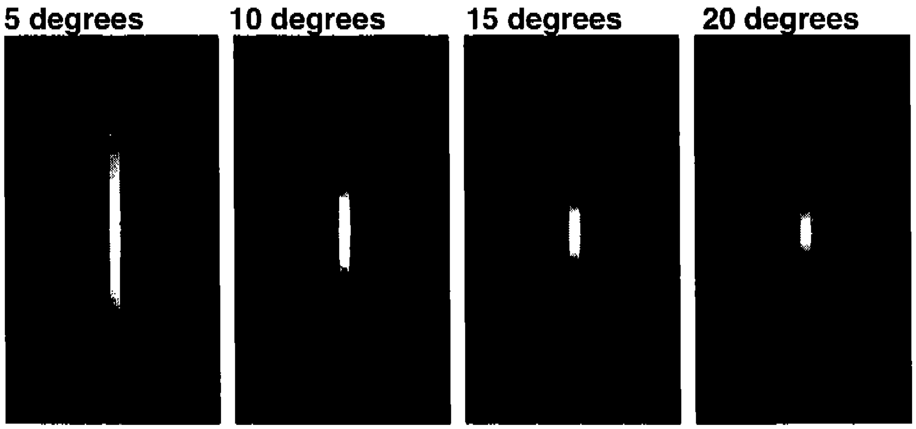

Figure 5. Images normal to the detector face for reconstructions of a point source with various acceptance angles. The detectors would be positioned at the top and bottom of each image.

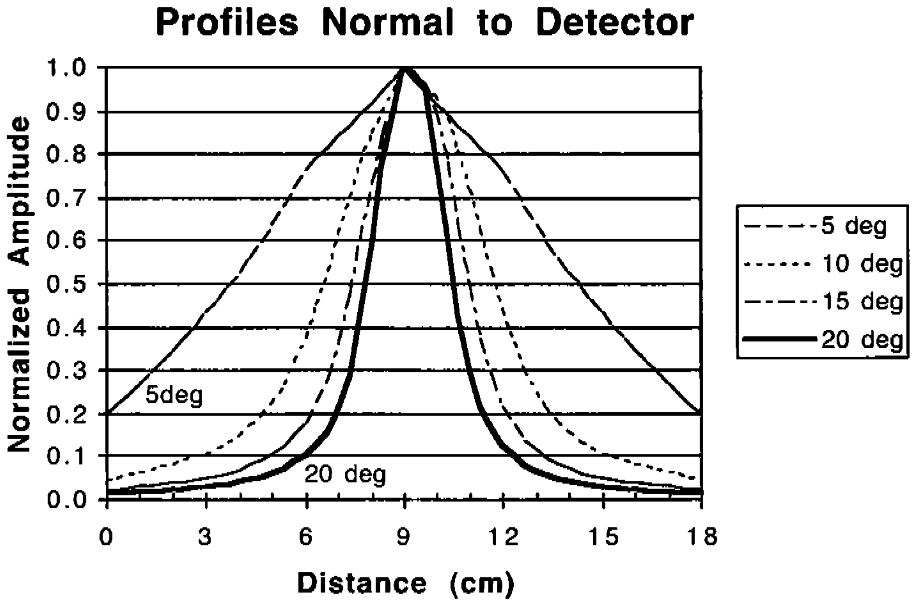

Figure 6. Profiles normal to the detectors for a point source simulation and image reconstruction with different acceptance angles. The images corresponding to these curves are shown in Figure 5.

A (10 degree acceptance angle)

B (20 degree acceptance angle)

Figure 7. Images of line sources from an experimental acquisition for (a) 10 degree and (b) 20 degree acceptance angles. (left) Focal plane image parallel to the detectors, (center) image normal to the detectors and (right) vertical profile through the center line source of the image normal to the detectors. Only the center 21 slices spaced at 3.3 mm were reconstructed.

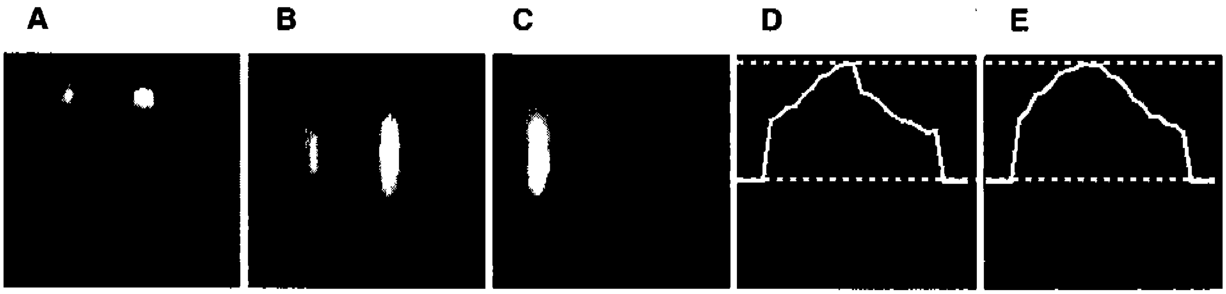

Figure 8. Images of a compressed breast phantom with simulated tumors from an experimental acquisition. Image reconstruction was with a 20 degree acceptance angle. (a) Focal plane image parallel to the detectors, (b) image normal to the detectors through the upper two tumors of (a), (c) image normal to the detectors through the tumors on the right side of (a), (d) vertical profile through the left tumor of (b), (e) vertical profile through the right tumor of (b).

A Classical Tomography (Backprojection)

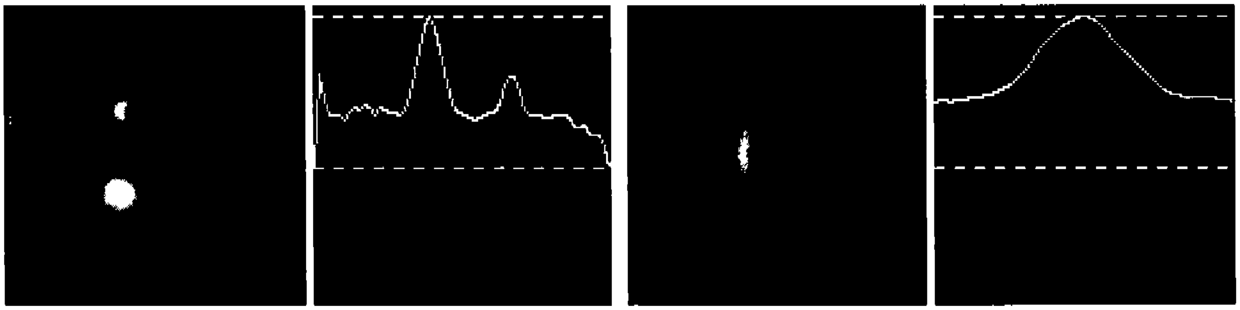

B Iterative MLEM

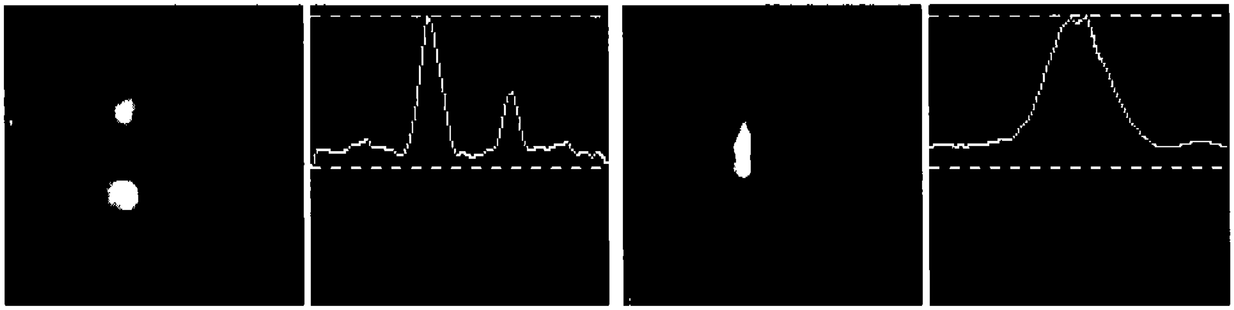

Figure 9. Images of a compressed breast phantom reconstructed with (a) classical tomography (backprojection) and (b) iterative MLEM (5 iterations) methods. From left to right: image through the simulated lesions parallel to the detectors, horizontal profile through the upper 12 and 9 mm diameter lesions, image normal to the detectors through the 12 and 9 mm lesions and a vertical profile through the 12 mm lesion.